

Measurement and analysis of dissolution patterns in rock fractures

Peter Erik Dijk¹ and Brian Berkowitz

Department of Environmental Sciences and Energy Research, Weizmann Institute of Science, Rehovot, Israel

Yoseph Yechieli

Geological Survey of Israel, Jerusalem, Israel

Received 29 September 2000; revised 20 September 2001; accepted 20 September 2001; published 19 February 2002

[1] Nuclear magnetic resonance imaging (NMRI) is applied to noninvasively measure flow and dissolution patterns in natural, rough-walled, water-saturated halite fractures. Three-dimensional images of water density and flow velocity acquired with NMRI allow quantification of the developing fracture morphology and flow patterns. The flow patterns are correlated strongly to the local apertures and the large-scale wall roughness. The correlations of the dissolution patterns to the fracture morphology, flow patterns, and mineralogical composition of the rock matrix are a function of the overall dimensionless Damköhler number. At high Damköhler numbers the dissolution patterns are dominated by the flow structure. In addition, at high Damköhler numbers buoyancy (stratified flow) becomes important. In such cases the dissolution patterns also depend on the orientation and elevation of the fracture walls, resulting in preferential upward dissolution. At low Damköhler numbers the dissolution patterns depend mainly on the mineralogical composition of the rock matrix. These findings suggest that coupled flow and dissolution processes are much more complex and unpredictable than commonly assumed, even under simplified conditions. *INDEX TERMS*: 1010 Geochemistry: Chemical evolution; 1832 Hydrology: Groundwater transport; 5114 Physical Properties of Rocks: Permeability and porosity; 5139 Physical Properties of Rocks: Transport properties; *KEYWORDS*: rock, fracture, flow, transport, dissolution, nuclear magnetic resonance imaging

1. Introduction

[2] Dissolution and precipitation processes are of prime importance in subsurface hydrology. They alter the structure and hydraulic properties of porous and fractured geological formations at various temporal and spatial scales. Treatment of field-scale problems is predicated on investigation of these processes at the laboratory scale, on formulation of conceptual and theoretical models, and on use of numerical simulations. In particular, studies of flow, dissolution, and precipitation in fractured formations are founded on analysis of the controlling mechanisms of these processes in single fractures [e.g., Dijk and Berkowitz, 1999; Dijk et al., 1999, and references therein].

[3] Flow and rock-water interactions in rough-walled rock fractures are extremely complex, even under laminar flow conditions. Furthermore, measurement of these interactions inside opaque rocks is prohibitively difficult. As a result, few (often indirect) quantitative observations exist. Moreover, the observational studies that currently exist have tended to emphasize experimental methods, such as scanning electron and optical microscopy, X-ray diffraction, and X-ray emission spectroscopy [e.g., Durham et al., 2001; Cooper, 1986, 1998; Gong et al., 1998; Moore et al., 1994; Blanpied et al., 1992; Johnson, 1981, 1992; Turpault et al., 1992a, 1992b; Vaughan et al., 1986], rather than the implications of the measurements or parameter values suitable

for input to quantitative models. Nuclear magnetic resonance imaging (NMRI) is another useful measurement technique, which allows the direct measurement of water densities and flow velocities in opaque aqueous samples. The efficacy of NMRI for studies of fractured media has been demonstrated by, for example, Dijk and Berkowitz [1999, 2000], Dijk et al. [1999], Brown et al. [1998], and Kumar et al. [1997].

[4] Ultimately, quantitative predictive models are required. Existing numerical models [e.g., Kaufmann and Braun, 1999; Dijk and Berkowitz, 1998; Hanna and Rajaram, 1998; Bécri et al., 1997; Dreybrodt, 1990, 1996; Gong et al., 1998; Mourzenko et al., 1996; Lowell et al., 1993; Berger et al., 1992], however, are highly idealized and rely on unvalidated assumptions and simplifications. Such models rarely, if ever, incorporate the effects of buoyancy, stratified flow, and mineralogy on flow and dissolution patterns. However, significant buoyancy effects, and thus stratified flow, can be expected even for relatively small solute concentration gradients. Consequently, for example, fractures may dissolve and collapse far more rapidly than predicted by these models. Moreover, the mineralogy of the rock matrix may have a significant influence on the dissolution rates in certain transport regimes. A particular case, where dissolution of soluble rock is driven by freshwater, fed by vertical fractures in adjacent insoluble rock (even for relatively distant freshwater sources), was investigated by Anderson and Kirkland [1980] in the field and in the laboratory using simplified channel geometries. Also, a preliminary study of halite fracture dissolution using NMRI, focusing on the geological issues related to dissolution in evaporite formations, was presented by Dijk and Berkowitz [2000].

[5] Notwithstanding the insight gained from previous studies, there remains significant uncertainty regarding the controlling

¹Now at School of Civil and Environmental Engineering, Georgia Institute of Technology, Atlanta, Georgia, USA.

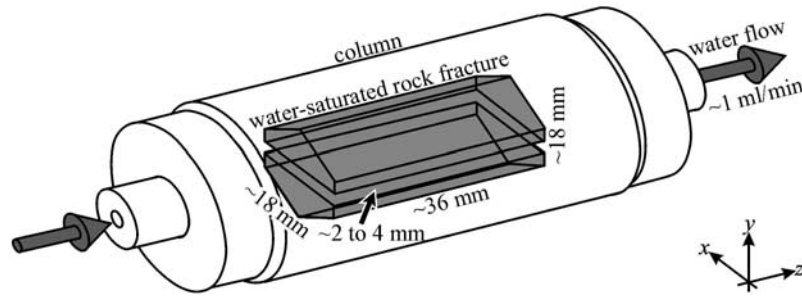


Figure 1. Experimental setup: a fractured rock sample, saturated with aqueous saline solution, mounted inside the polytetrafluoroethylene column.

mechanisms of combined flow, dissolution and precipitation, their interactions, and their effects on the properties of geological formations. No direct, noninvasive, three-dimensional, high-resolution measurements of flow, dissolution, and precipitation in natural rock fractures exist. The objective of this study is to promote the understanding of the complex flow and rock-water interactions and to analyze assumptions underlying existing predictive flow and transport models. For this purpose, NMRI is applied to visualize the dynamic behavior of coupled flow and dissolution in natural, rough-walled, water-saturated rock fractures.

2. Methodology

[6] Most technical details of the experimental setup and application of the NMRI technique are discussed in detail by *Dijk et al.* [1999]. Sections 2.1 and 2.2 provide a brief summary of the major issues, and section 2.3 describes the mineralogical analysis of the source rock.

2.1. Experimental Setup

[7] A schematic of the experimental setup is presented in Figure 1. Relatively planar, rough fractures were induced along the width of natural halite samples. Each sample has a height and width of ~ 18 mm and a length of ~ 36 mm. The mean aperture was set at ~ 2 mm, which is convenient for NMRI measurements. The fractured rock samples were mounted in cylindrical polytetrafluoroethylene (PTFE) columns so that the only flow passage was the fracture. Deionized water, fully saturated with the rock matrix components (sodium chloride) to prevent fracture wall dissolution, flowed through the columns driven by a peristaltic pump. The mean velocity of the saline aqueous solution in the fractures was set at ~ 1 mm s^{-1} , representative of groundwater flow in many natural rock fracture systems. Pulses of undersaturated saline solution in between NMRI measurements were applied to induce dissolution of the rock fracture walls. The inflowing solute content of these pulses was used to adjust the dissolution rates. Two sealed polyvinylchloride (PVC) tubes with inner diameters of ~ 1.6 mm containing the fully saturated saline solution were mounted in each column to serve as a zero-velocity reference.

[8] Three different halite fracture systems were investigated. They vary in fracture orientation (horizontal and vertical), temporal mean of the applied volumetric flow rate $\langle Q \rangle_t$, and solute content of the inflowing pulse c_{in}/c_{sat} ($c_{in}/c_{sat} = 0$ for pure water and $c_{in}/c_{sat} \approx 0.5$ for $\sim 50\%$ saturated saline solution). As a result, the time intervals between NMRI measurements Δt , the number of images in the time series i_{tot} , and therefore the total

dissolution times $t_{tot} = i_{tot}\Delta t$ differ. The choice of Δt was such that the change in fracture walls was detectable yet minimal. The dissolution experiments ceased when the saline solution flowing through the rock fractures came into contact with the sealing material surrounding the rock samples. The orientation of the principal flow direction is horizontal for all three fracture systems. The experimental parameters for the fracture systems are given in Table 1.

[9] The overall dimensionless Damköhler number Da' , which is a measure of dissolution versus flow rate, is used to qualitatively describe the overall dissolution rates. Note that a generic definition of the Damköhler number is given by, for example, $Da = k_n c^{n-1} / (v/L)$, where k_n is the kinetic reaction coefficient for an n th-order reaction, c is the solute concentration, v is the fluid flow velocity, and L is the characteristic length scale. High Da' indicates the inflow of pure water ($c_{in}/c_{sat} = 0$), while low Da' indicates the inflow of $\sim 50\%$ saturated saline solution ($c_{in}/c_{sat} \approx 0.5$).

2.2. NMRI

[10] The samples were inserted in a horizontal, cylindrical proton radio frequency probe inside a horizontal, cylindrical static electromagnet bore operating at a field strength of 4.7 T. The classical NMRI phase imaging approach, i.e., a three-dimensional (3-D) flow-encoded spin echo pulse sequence [e.g., *Moran*, 1982], was applied. This sequence allows the measurement of water densities and selected flow velocity components [*Dijk et al.*, 1999]. By combining velocity components for three perpendicular directions, 3-D velocity vectors can be obtained. In this study, 3-D distributions, i.e., a one-dimensional (1-D) profile in the y direction at each location (x, z) , of the 1-D velocity component in the principal flow (z) direction were investigated.

[11] The pulse sequence was calibrated extensively [*Dijk et al.*, 1999]. The reproducibility of the measurements was confirmed by analyzing rapid successions of two-dimensional (2-D) images with relatively short acquisition times.

Table 1. Experimental Parameters for the Three Fracture Systems

	Sample		
	1	2	3
Fracture orientation	horizontal	horizontal	vertical
$\langle Q \rangle_t$, mL min^{-1}	1.083 ± 0.006	1.04 ± 0.01	0.990 ± 0.007
c_{in}/c_{sat}	0.0	0.5	0.0
Δt , min	1	5	1
i_{tot}	9	8	9
t_{tot} , min	8	35	8

Table 2. NMRI Parameters for the Three Fracture Systems^a

	Sample		
	1	2	3
xyz, mm^3	$21 \times 21 \times 32$	$23 \times 23 \times 32$	$21 \times 21 \times 32$
$\Delta x \Delta y \Delta z, \text{mm}^3$	$0.16 \times 0.16 \times 0.25$	$0.18 \times 0.18 \times 0.25$	$0.16 \times 0.16 \times 0.25$
$n_x n_y n_z$	$74 \times 56 \times 57$	$51 \times 35 \times 58$	$42 \times 63 \times 58$

^aDefinitions are as follows: xyz , field of view; $\Delta x \Delta y \Delta z$, spatial resolution; $n_x n_y n_z$, matrix subset; and x, y , and z , spatial coordinates along fracture width, height, and length, respectively.

[12] The images have a matrix of $128 \times 128 \times 128$. The spatial field of view and thus the spatial resolution vary slightly between samples. Only a subset of the matrix that contains the actual fracture volume was analyzed. The NMRI parameters for the three fracture systems are given in Table 2. The resolution of the velocities is $\sim 0.025 \text{ mm s}^{-1}$. A relatively short acquisition time of ~ 1 hour 12 min per image was made possible by introducing a nuclear magnetic relaxation agent, i.e., $\sim 5 \text{ mM NiCl}_2(\text{aq})$, to the aqueous solution. To measure the dissolution processes with time-scales of minutes using NMRI with acquisition times of the order of an hour, the following procedure was employed: (1) Pure water or $\sim 50\%$ saturated saline solution was pumped through the fracture during time intervals Δt (Table 1) to invoke dissolution of the rock matrix. (2) Fully saturated saline solution was pumped through the fracture during the NMRI acquisition time to inhibit dissolution during the actual measurements. This procedure is then

repeated. Thus the measured flow patterns do not refer to those during the actual dissolution process.

2.3. Mineralogical Analysis of Source Rock

[13] The rock samples were obtained from Mount Sedom, which is a salt diapir located to the west of the Dead Sea in Israel. The salt originates from marine ingression at Neogene times [Zak, 1967] that precipitated the Sedom formation. This formation is composed mainly of halite (NaCl , $\sim 96\%$ of the whole rock) but also contains minor amounts of calcium sulfates (anhydrite CaSO_4 and gypsum $\text{CaSO}_4 \cdot 2\text{H}_2\text{O}$), carbonates (e.g., dolomite $\text{CaMg}(\text{CO}_3)_2$ and some calcite CaCO_3), potassium and magnesium salts (e.g., sylvite KCl and carnallite $\text{KMgCl}_3 \cdot 6\text{H}_2\text{O}$), and quartz and clays [Zak, 1967]. These minor minerals may occur as discrete thin layers or dispersed within the halite [Zak, 1967]. Chemical impurities can exist in various forms, for example, as embedded or absorbed macroscopic phases, microscopic fluid inclusions, and ionic crystal substitutions.

[14] The dissolution and precipitation rates depend on, for example, the mineralogical composition of the rock matrix and the chemical composition of the aqueous solution, the rock-solution interface area, the thickness of the diffusional layer adjacent to the interface, the occurrence of surface coatings, the temperature, and the flow conditions. The dissolution rates and saturation contents (solubilities) of different constituents in water vary considerably. For example, they equal $\sim 0.02 \times 10^{-2} \text{ kg m}^{-2} \text{ s}^{-1}$ [Alkattan et al., 1997] and $\sim 4 \times 10^2 \text{ kg m}^{-3}$ [Windholz, 1976], respectively, for halite and a factor of ~ 15 [Raines and

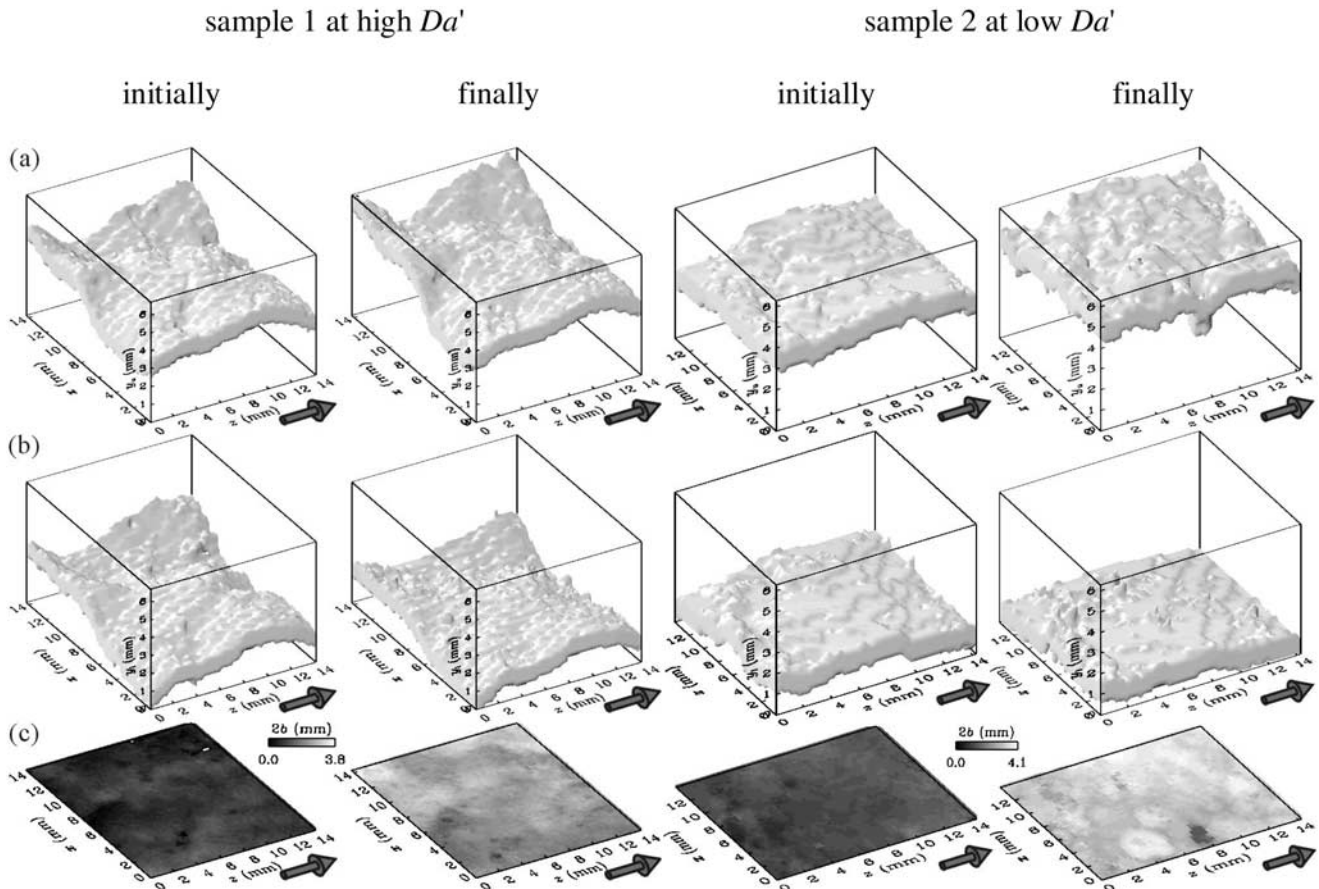


Figure 2. Initial and final fracture morphology: (a) upper wall locations y_1 , (b) lower wall locations y_0 and (c) apertures $2b$ for sample 1 at high Da' and sample 2 at low Da' .

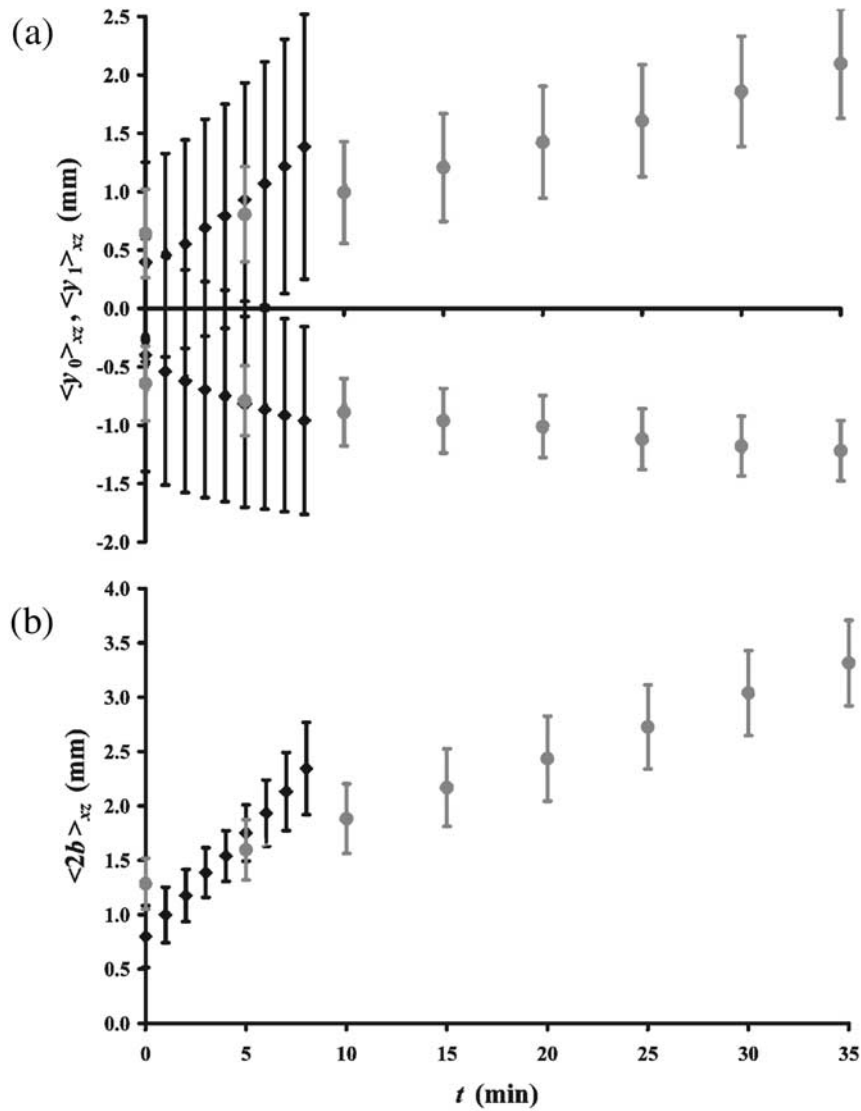


Figure 3. Developing fracture morphology: (a) spatial means of upper and lower fracture wall locations $\langle y_1 \rangle_{xz}$ and $\langle y_0 \rangle_{xz}$ and (b) fracture apertures $\langle 2b \rangle_{xz}$ as a function of time t (symbols) including their standard deviations (error bars). Results for sample 1 at high Da' are shown as solid, and results for sample 2 at low Da' are shown as shaded.

Dewers, 1997] and ~ 0.005 [Ohmoto *et al.*, 1991] as much for gypsum at $\sim 25^\circ\text{C}$. Thus, while larger amounts of halite than gypsum can be dissolved in water, gypsum dissolves more rapidly than halite.

[15] The content of halite, calcium sulfate, and other minor elements of the water-soluble phase of the halite samples was determined by chemical analysis. The elements Na, Ca, SO_4 , K, Mg, and Sr were analyzed by inductively coupled plasma (ICP), and Cl was analyzed by titration. The presence of halite, anhydrite, calcium carbonate, and quartz in these samples was also examined by mineralogical analysis using X-ray diffraction (XRD). The chemical and mineralogical composition of the water-insoluble phase (e.g., clay) was not determined. The extent of the variation of the mineralogical composition was determined by examining the source rock from which the samples were cut. Several distinct types of halite were classified on the basis of the visual observation of color and texture. Chemical and mineralogical analysis was performed on samples of these rock types. In addition, chemical

analysis was performed on halite from two parts of the residual halite samples after completion of each of the experiments.

3. Results

3.1. Developing Fracture Morphology

[16] The fracture morphology and its changes can be characterized by, for example, the wall locations, apertures, cross-sectional areas, volumes, center locations, and critical aperture regions. The current analysis of the morphology focuses on the horizontally oriented fractures (samples 1 and 2) and to a lesser extent on the vertically oriented fracture (sample 3). The morphology (the lower and upper wall locations y_0 and y_1 and the aperture $2b = y_1 - y_0$, at all (x, z) locations) for the initial and the final states of the horizontal fractures (sample 1 at high Da' and sample 2 at low Da') are presented in Figure 2. For dissolution, y_0 decrease, and y_1 and $2b$ increase at all (x, z) locations. Only the initial and final morphologies are shown, and the ranges of the gray scales are selected for comparison between

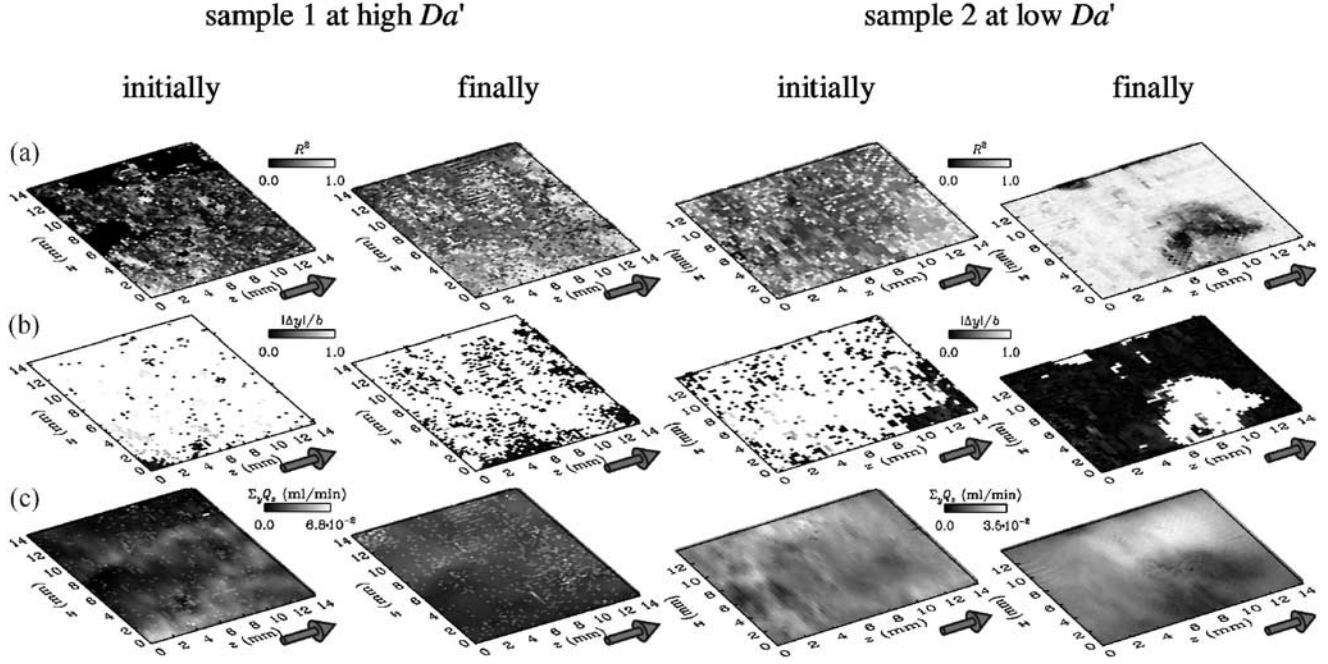


Figure 4. Initial and final liquid flow patterns: (a) linear correlation coefficients R^2 for more than four data points $n > 4$, (b) absolute relative y direction offsets $|\Delta y|/b$ for more than four data points $n > 4$ and $R^2 > 0.7$, and (c) volumetric flow rates $\Sigma_y Q_z$ for sample 1 at high Da' and sample 2 at low Da' .

the initial and final morphology. This does not reveal the full development of the morphology and all the correlations involved. The selection of other ranges may display other features. The measurement error for y_0 and y_1 is $\sim \Delta y \approx 0.13$ mm.

[17] Note that from this point forward, the subscripts to the right of the average shown by angle brackets, standard deviation σ , summation Σ , and gradient ∇ symbols indicate the coordinates (x , y , z , and t) over which these operators have been applied. For example, $\langle \nabla_t y_0 \rangle_{xz}$ represents the spatial mean of the temporal gradient of y_0 averaged over the xz plane of the fracture. When constant, the values are presented in the form $\langle v \rangle = m \pm s$, where m is the mean and s is the standard deviation of the variable v . In some cases, reported distributions overlap. These distributions, however, may still be considered as distinct: While it might not be possible to distinguish with reasonable certainty the distribution to which individual data points belong, differences between data sets that define the distributions are clearly discernible.

[18] The spatial means of the lower and upper wall locations $\langle y_1 \rangle_{xz}$ and $\langle y_0 \rangle_{xz}$ and the apertures $\langle 2b \rangle_{xz}$ as a function of time t for the horizontal fractures (sample 1 at high Da' and sample 2 at low Da') are presented in Figure 3. For dissolution, $\langle y_0 \rangle_{xz}$ decreases, and $\langle y_1 \rangle_{xz}$ and $\langle 2b \rangle_{xz}$ increase.

3.2. Developing Flow Patterns

[19] The flow patterns and their changes can be characterized by, for example, the velocities and their profiles (their parabolic shape and asymmetry), flow rates, and critical flow rate regions. The 3-D velocity distribution v_z can be characterized by the velocity averaged over the y direction $\langle v_z \rangle_y = \Sigma_y v_z \Delta y / (2b)$. The 3-D distribution of the volumetric flow rates $Q_z = v_z \Delta x \Delta y$ can be integrated over the y direction $\Sigma_y Q_z = \langle v_z \rangle_y \Delta x 2b$ and over the xy plane perpendicular to the principal flow (z) direction $\Sigma_{xy} Q_z$. The velocity profiles between the fracture walls in the y direction are characterized by their parabolic shape and asymmetry.

[20] The parabolic shape of the velocity profiles is described by the linear correlation coefficient R^2 between the velocity profiles and their least mean squares parabolic fits. This is only relevant for more than four data points per velocity profile $n > 4$ and for parabolic fits that are positively correlated to the velocity profiles ($R > 0$; otherwise, R^2 is set to 0). For perfectly parabolic velocity profiles, $R^2 = 1$, and for completely nonparabolic velocity profiles, $R^2 = 0$.

[21] The asymmetry of the velocity profiles with respect to the fracture center or the fracture walls is described by the relative offset in the y direction $\Delta y/b$ of the least mean squares parabolic fits. It is only relevant if the maximum velocity of the parabolic fits fall within the fracture space (i.e., $-1 < \Delta y/b < 1$). For perfectly centered fits of the velocities $\Delta y/b = 0$ and for completely offset fits (the maximum velocity is adjacent to one of the fracture walls), $|\Delta y/b| = 1$. Only for more than four data points per velocity profile $n > 4$ and for reasonably parabolic fits (say, with $R^2 > 0.7$) is $\Delta y/b$ meaningful.

[22] The flow patterns (characterized by the linear correlation coefficient between the velocity profiles and their least mean squares parabolic fit R^2 , the absolute relative offset or asymmetry in the y direction $|\Delta y|/b$, and the volumetric flow rate $\Sigma_y Q_z$) for the initial and final states of the horizontal fractures (sample 1 at high Da' and sample 2 at low Da') are presented in Figure 4. The current analysis of the flow patterns focuses on the horizontally oriented fractures and only to a lesser extent on the vertically oriented fracture. The range of the scale of $\Sigma_y Q_z$ (Figure 4c) for sample 1 is nearly twice that of sample 2. As in section 3.1, only the initial and final flow patterns are shown, and the ranges of the gray scales are selected for comparison between the initial and final flow patterns. The measurement error for the velocity component in the z direction v_z is ~ 0.025 mm s $^{-1}$ (section 2.2).

[23] The spatial means of the velocities $\langle v_z \rangle_{xyz}$, the flow rates $\langle \Sigma_y Q_z \rangle_{xz}$, the linear correlation coefficients $\langle R^2 \rangle_{xz}$, and the relative

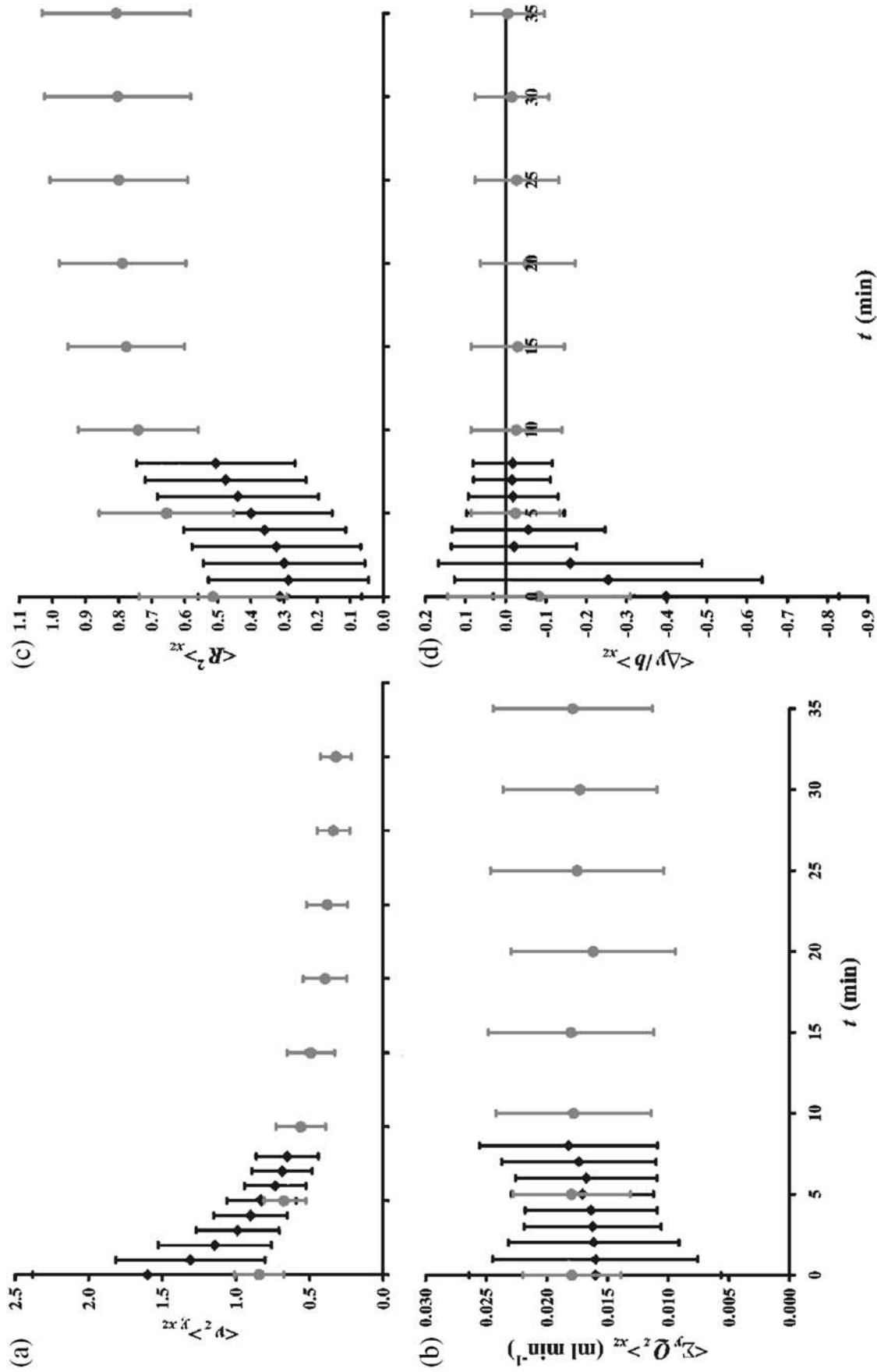


Figure 5. Spatial means of (a) velocities $\langle \bar{v}_z \rangle_{xz}$, (b) flow rates $\langle \bar{Q}_z \rangle_{xz}$, (c) linear correlation coefficients $\langle R^2 \rangle_{xz}$, and (d) relative offsets $\langle \Delta y/b \rangle_{xz}$ as a function of time t (symbols) including their standard deviations (error bars). Results for sample 1 at high Da' are shown as solid, and results for sample 2 at low Da' are shown as shaded.

offsets $\langle \Delta y/b \rangle_{xz}$ as a function of time t for sample 1 at high Da' and for sample 2 at low Da' are presented in Figure 5.

4. Discussion

[24] The 3-D distributions of water densities and flow velocities were obtained without any underlying assumptions or simplifications and in directly accessible, digital form. These measurements permit analysis of the evolution of the fracture morphology and flow patterns. The relevant parameters can be characterized by a considerable number of coordinates, variables, operators, and correlations, which results in a large quantity of data. Their summary, consisting of the principal results, is presented in the subsequent sections. The discussion focuses on (1) the relationship between the flow patterns and the fracture morphology, (2) the flow regimes in the fracture, and (3) the dissolution patterns in terms of the changing fracture morphology, the dissolution regimes, and the evolving flow patterns.

4.1. Flow Patterns Versus Fracture Morphology

[25] Flow patterns depend on the fracture morphology. Here the relationships between the flow rates and the apertures and the geometric tortuosity are investigated.

4.1.1. Flow rates versus apertures. [26] The relationships between the flow rates versus the apertures can be characterized from direct observations and by the overlap between their critical regions, their power law relationship, and the local cubic law (LCL).

4.1.1.1. Direct observations: [27] Although it is not necessarily evident by comparing Figures 4c and 2c, the flow rates $\Sigma_y Q_z$ are often correlated to the apertures $2b$. For example, for the initial state of sample 1, high $\Sigma_y Q_z$ at low x and z correspond to high apertures $2b$. Also, for the initial and final states of sample 2, high $\Sigma_y Q_z$ at high x correspond to high $2b$. Thus significant correlations between $\Sigma_y Q_z$ and $2b$ can be observed.

4.1.1.2. Overlap between critical regions: [28] The critical aperture region $(2b)_c$ is defined here as the set of surface area elements $\Delta x \Delta z$ that contain a set of apertures $2b$ exceeding a critical value, are connected to each other, and critically link the inflow side to the outflow side of the fracture. To locate $(2b)_c$, surface area elements with decreasing $2b$ (starting with the maximum aperture $2b_{\max}$) are added to the set, and a search algorithm is used to determine whether the connected part of this set links the inflow side to the outflow side of the fracture. The minimum $2b$ contained in $(2b)_c$, i.e., the latest addition to the set to make it a critical region, is called the critical aperture $2b_c$. Thus all $2b$ in $(2b)_c$ are greater than or equal to $2b_c$. The critical flow rate region $(\Sigma_y Q_z)_c$ and the critical flow rate $\Sigma_y Q_{z|c}$ are defined likewise. Note that $\Sigma_y Q_{z|c}$ can be a measure of the preferential flow path. The overlap between $(2b)_c$ and $(\Sigma_y Q_z)_c$ is described by the ratios between the overlapping surface area and the union surface area of the critical regions $\alpha_{c,u} = A_{(\Sigma_y Q_z)_c} \cap A_{(2b)_c} / A_{(\Sigma_y Q_z)_c} \cup A_{(2b)_c}$. For sample 1 at high Da' , $\alpha_{c,u}$ remain constant in time at $\langle \alpha_{c,u} \rangle_t \approx 0.4 \pm 0.2$, and for sample 2 at low Da' , $\alpha_{c,u}$ remain constant in time at $\langle \alpha_{c,u} \rangle_t \approx 0.41 \pm 0.06$. This indicates that there is significant overlap between $(2b)_c$ and $\Sigma_y Q_{z|c}$. Thus $(2b)_c$ can predict, to a certain extent, $(\Sigma_y Q_z)_c$.

4.1.1.3. Power law: [29] The flow rates $\Sigma_y Q_z$ are correlated to the apertures $2b$, as indicated by the linear strengths c_0 of their cross correlations. For the cross correlations between $\log(\Sigma_y Q_z)$ and $\log(2b)$, c_0 remain constant in time at $\langle c_0 \rangle_t \approx 0.70 \pm 0.08$ for sample 1 at high Da' , and c_0 decrease from ~ 0.60 to ~ 0.47 for sample 2 at low Da' . Thus a power law $\log(\Sigma_y Q_z) \propto C_1 \log(2b)$

[Dijk and Berkowitz, 1999] with an exponent C_1 can be used to describe this overall relationship. Using linear regression, it was found that for sample 1 at high Da' , C_1 remain constant in time at $\langle C_1 \rangle_t \approx 1.2 \pm 0.2$ and the linear correlation coefficients R^2 remain constant in time at $\langle R^2 \rangle_t \approx 0.98 \pm 0.01$. For sample 2 at low Da' , C_1 remain constant in time at $\langle C_1 \rangle_t \approx 0.9 \pm 0.2$, and R^2 remain constant in time at $\langle R^2 \rangle_t \approx 0.87 \pm 0.08$. Thus $\Sigma_y Q_z$ can be predicted from $2b$ with a certain degree of accuracy. Note that the observed overall mean behavior of the power law is not necessarily valid locally for individual data points.

[30] The local spatial hydraulic head gradients ∇h are unknown. Therefore it is not possible to further compare the results here to those of the LCL, which assumes parabolic and symmetric velocity profiles to predict the flow rates from the apertures, $\Sigma_y Q_z \propto (2b)^3$. Thus what is important is not the actual values of C_1 but the fact that they are significantly greater than zero. The positive correlations between $\Sigma_y Q_z$ and $2b$ could be observed without considering ∇h , because the variations of ∇h are expected to be of the same order of magnitude as, or smaller than, the variations of $2b$. In addition, the power law is found to be valid for the entire range of $\Sigma_y Q_z$ and $2b$, because no distinct low- and high-flow regions exist in these fractures. Such high-flow regions could behave essentially like 1-D flow systems with minimal tortuosity effects.

4.1.1.4. Comparison to local cubic law (LCL): [31] A measure of the predictability of the flow rates is the ratio β between the effective half aperture $b_{\text{eff},x}$ (based on the observed flow rates, $b_{\text{eff},x} = \{\Sigma_{xy} Q_z [\Sigma_x (\Sigma_y Q_z / b^3)]^{-1}\}^{1/3}$) and the effective LCL half aperture $b_{\text{eff,LCL},x}$ (based on the assumption of perfectly parabolic, symmetric velocity profiles, $b_{\text{eff,LCL},x} = ((b^3)_x)^{1/3}$) in the xy plane perpendicular to the principal flow (z) direction [Dijk and Berkowitz, 1999; Dijk et al., 1999], $\beta = b_{\text{eff},x} / b_{\text{eff,LCL},x} = \{\Sigma_{xy} Q_z [\Sigma_x (\Sigma_y Q_z / b^3)]^{-1} (b^3)_x^{-1}\}^{1/3}$.

[32] For sample 1 at high Da' the spatial mean of the ratio $\langle \beta \rangle_z$ remains constant in time at $\langle \beta \rangle_{zt} \approx 0.93 \pm 0.07$, while for sample 2 at low Da' , $\langle \beta \rangle_z$ increases from $\sim 0.96 \pm 0.03$ to $\sim 0.98 \pm 0.03$. The fact that $\langle \beta \rangle_z$ remains slightly less than unity indicates that the measured flow rates remain slightly less than the LCL flow rate predictions (in agreement with numerical simulations of flow through rough-walled channels [e.g., Mourzenko et al., 1996]), especially at high Da' . The strengths of the spatial autocorrelations of β remain small, which indicate that the deviations from the LCL flow rate predictions are local phenomena. Thus the LCL tends to slightly overestimate the flow rates.

4.1.2. Flow rates versus geometric tortuosity. [33] The fracture center location $y_m = \frac{1}{2}(y_1 + y_0)$ is a measure of the fracture orientation. Large variations in y_m and apertures $2b$ (especially when these variations occur locally at the same position) indicate significant wall roughness and discontinuities and thus potentially geometric tortuosity. Significant spatial variations of y_m (see y_0 and y_1 in Figures 2a and 2b) and $2b$ (Figure 2c) occur in relatively small areas (i.e., locally) at the same position for sample 2 at low Da' but not for sample 1 at high Da' . In particular, for sample 2 the region with only minor dissolution (at low x and medium z) creates significant geometric tortuosity and strongly affects the flow patterns (Figure 4). Thus, while the flow rates are primarily determined by $2b$ (as predicted by the LCL, see section 4.1.1), the geometric tortuosity also plays a very important role.

4.2. Flow Regimes

[34] The flow patterns are characterized by the dimensionless Reynolds number, which is a measure of inertial versus viscous

forces. The Reynolds number is defined here as $Re_z = 2b\rho v_z/\mu$, where $2b$ is the fracture aperture, v_z is the velocity in the principal flow (z) direction, ρ is the density, and μ is the dynamic viscosity of the liquid. The Reynolds number averaged over the y direction $\langle Re_z \rangle_y = 2b\rho\langle v_z \rangle_y/\mu = \rho\Sigma_y Q_z/(\mu\Delta x)$ is directly proportional to the volumetric flow rate $\Sigma_y Q_z$ and thus behaves accordingly. For a fully saturated saline solution, $\rho \approx 1.20 \times 10^3 \text{ kg m}^{-3}$, and $\mu \approx 1.99 \times 10^{-3} \text{ kg m}^{-1} \text{ s}^{-1}$ [Wolf et al., 1975]. For sample 1 at high Da' the spatial means of the Reynolds numbers $\langle Re_z \rangle_{xyz}$ increases from 0.8 ± 0.5 to 0.9 ± 0.4 , while for sample 2 at low Da' , $\langle Re_z \rangle_{xyz}$ remains constant in time at $\langle Re_z \rangle_{xyz} \approx 0.63 \pm 0.02$. Thus $\langle Re_z \rangle_{xyz}$ remains of the order of ~ 1 . This indicates that the flow remains generally laminar (since $\langle Re_z \rangle_{xyz}$ is much smaller than the critical Reynolds number Re_{cr} , i.e., $\langle Re_z \rangle_{xyz} \ll Re_{cr} \approx 2.1 \times 10^3$ [Bird et al., 1960], for flow between two planar, parallel, smooth plates), as assumed by the LCL (see section 4.1.1). However, in the vicinity of the rough walls the flow may well be nonlaminar, and the LCL may not be valid. In addition, the nonlaminar flow can also have a significant influence on solute transport and thus on dissolution and precipitation rates.

[35] The dimensionless Péclet number is a measure of flow versus molecular diffusion rates. It is defined here as $Pe_z = 2bv_z/D_m$, where D_m is the diffusion coefficient. The Péclet number averaged over the y direction $\langle Pe_z \rangle_y = 2b\langle v_z \rangle_y/D_m = \Sigma_y Q_z/(D_m\Delta x)$ is directly proportional to the volumetric flow rate $\Sigma_y Q_z$ and thus behaves accordingly. For a fully saturated saline solution, $D_m \approx 2.2 \times 10^{-9} \text{ m}^2 \text{ s}^{-1}$ [Alkattan et al., 1997]. With mean flow velocities of $\langle v_z \rangle \approx 1 \text{ mm s}^{-1}$ in the fractures with length $L \approx 36 \text{ mm}$ the mean residence time of the aqueous saline solution is $\langle \tau_v \rangle = L/\langle v_z \rangle \approx 36 \text{ s}$. In contrast, the mean diffusion time with respect to the mean fracture aperture of $2b \approx 2 \text{ mm}$ is $[(2b)^2/D_m] \approx 1.8 \times 10^3 \text{ s}$, which is a factor of ~ 50 greater. Thus it appears that the flow rates are much greater than the diffusion rates. For sample 1 at high Da' the spatial mean of the Péclet number $\langle Pe_z \rangle_{xyz}$ increases from $6 \times 10^2 \pm 4 \times 10^2$ to $7 \times 10^2 \pm 3 \times 10^2$, while for sample 2 at low Da' , $\langle Pe_z \rangle_{xyz}$ remains constant in time at $\langle Pe_z \rangle_{xyz} \approx 4.8 \times 10^2 \pm 0.2 \times 10^2$. Thus $\langle Pe_z \rangle_{xyz}$ remains of the order of $\sim 10^2$. This affirms that the diffusion rates remain negligible compared to the flow rates (since $\langle Pe_z \rangle_{xyz}$ is greater than the critical Péclet number Pe_{cr} , i.e., $\langle Pe_z \rangle_{xyz} > Pe_{cr} \approx 10$ [Berkowitz and Zhou, 1996]).

4.3. Dissolution Patterns

4.3.1. Changing fracture morphology. [36] Initially, the lower and upper wall locations y_0 and y_1 for samples 1 and 2 (Figures 2a and 2b) are well matched: No offset was added after inducing the fracture, and no significant pieces of the rock matrix were lost during the process of fracturing and mounting the sample. For sample 1 the spatial gradients of the wall locations are $\langle \nabla_x y_0 \rangle_{xzt} \approx 0.257 \pm 0.008$, $\langle \nabla_z y_0 \rangle_{xzt} \approx 0.243 \pm 0.007$, $\langle \nabla_x y_1 \rangle_{xzt} \approx 0.2 \pm 0.4$, and $\langle \nabla_z y_1 \rangle_{xzt} \approx 0.3 \pm 0.3$, while for sample 2, $\langle \nabla_x y_0 \rangle_{xzt} \approx 0.1 \pm 0.3$, $\langle \nabla_z y_0 \rangle_{xzt} \approx 0.2 \pm 0.3$, $\langle \nabla_x y_1 \rangle_{xzt} \approx 0.1 \pm 0.3$, and $\langle \nabla_z y_1 \rangle_{xzt} \approx 0.2 \pm 0.3$. In contrast, for sample 1 the spatial standard deviations of the wall locations are $\sigma_{y_0,xz} \approx 1.0$ and $\sigma_{y_1,xz} \approx 0.85$, while for sample 2, $\sigma_{y_0,xz} \approx 0.32$ and $\sigma_{y_1,xz} \approx 0.38$. Thus samples 1 and 2 are approximately equally rough at the small scale. However, at the large scale the walls of sample 1 are rougher than those of sample 2.

[37] The walls dissolve linearly (Figure 3a), which is also evident from the temporal gradients of the wall locations. For sample 1 at high Da' , $\langle \nabla_t y_0 \rangle_{xzt}$ decreases in magnitude from -0.14 ± 0.09 to $0.0 \pm 0.1 \text{ mm min}^{-1}$, and $\langle \nabla_t y_1 \rangle_{xzt}$ increases from 0.1 ± 0.1 to $0.2 \pm 0.1 \text{ mm min}^{-1}$, while for sample 2 at low Da' , $\langle \nabla_t y_0 \rangle_{xzt}$ and $\langle \nabla_t y_1 \rangle_{xzt}$ remain constant in time at

$\langle \nabla_t y_0 \rangle_{xzt} \approx -0.016 \pm 0.008 \text{ mm min}^{-1}$ and $\langle \nabla_t y_1 \rangle_{xzt} \approx 0.042 \pm 0.006 \text{ mm min}^{-1}$, respectively. Thus they dissolve more rapidly at high than at low Da' . At high Da' , y_0 dissolve decreasingly rapidly, while y_1 dissolve increasingly rapidly. At low Da' the walls dissolve at constant rates.

[38] For sample 1 at high Da' , $\langle \nabla_x y_0 \rangle_{xzt}$ and $\langle \nabla_z y_0 \rangle_{xzt}$ remain constant in time at $\langle \nabla_x y_0 \rangle_{xzt} \approx 0.257 \pm 0.008$ and $\langle \nabla_z y_0 \rangle_{xzt} \approx 0.243 \pm 0.007$, respectively, and $\langle \nabla_x y_1 \rangle_{xzt}$ increases from 0.2 ± 0.4 to 0.3 ± 0.4 , and $\langle \nabla_z y_1 \rangle_{xzt}$ changes from 0.3 ± 0.3 to 0.3 ± 0.4 . For sample 2 at low Da' , $\langle \nabla_x y_0 \rangle_{xzt}$ increases from 0.1 ± 0.3 to 0.2 ± 0.4 , $\langle \nabla_z y_0 \rangle_{xzt}$ changes from 0.2 ± 0.3 to 0.2 ± 0.5 , $\langle \nabla_x y_1 \rangle_{xzt}$ increases from 0.1 ± 0.3 to 0.3 ± 0.4 , and $\langle \nabla_z y_1 \rangle_{xzt}$ increases from 0.2 ± 0.3 to 0.4 ± 0.6 . In contrast, for sample 1 at high Da' , $\sigma_{y_0,xz}$ decreases from 1.0 to 0.80 and $\sigma_{y_1,xz}$ increases from 0.85 to 1.1, while for sample 2 at low Da' , $\sigma_{y_0,xz}$ decreases from 0.32 to 0.26 and $\sigma_{y_1,xz}$ increases from 0.38 to 0.47. Thus, in general, the more rapidly the walls dissolve, the rougher they become at the small scale: The small scale roughness of y_0 remains approximately constant, while y_1 become rougher.

[39] Finally, y_0 and y_1 retain most of their large-scale features (Figures 2a and 2b). They dissolve uniformly, except for y_1 at low Da' with almost no dissolution at low x and medium z . At high Da' , y_0 and y_1 remain well matched, while becoming less well matched at low Da' .

[40] Initially, the apertures $2b$ for samples 1 and 2 (Figure 2c) are uniform with mean values of ~ 0.8 and $\sim 1.3 \text{ mm}$, respectively. The fracture space (described by $2b$) increases highly linearly at constant rates, significantly more rapidly at high than at low Da' (Figure 3b). The fracture space (described by $2b$) remains much more complex than its bounding fracture walls (described by y_0 and y_1). Finally, $2b$ are nonuniform, especially for sample 1 at high Da' . For sample 1 at high Da' , $2b$ range from $\sim 2 \text{ mm}$ at low x to $\sim 4 \text{ mm}$ at high x , with small $2b \approx 1 \text{ mm}$ at low x and z . For sample 2 at low Da' , $2b \approx 4 \text{ mm}$, except at low x and medium z with small $2b \approx 1 \text{ mm}$. Slightly upflow of this region (at higher z), there are some distinct circular regions with large $2b \approx 4 \text{ mm}$.

4.3.2. Dissolution regimes. [41] Depending on Da' , several different dissolution regimes can be distinguished. At high Da' the dissolution patterns are dominated by the flow patterns. In addition, at high Da' , buoyancy (stratified flow) becomes important. At low Da' the dissolution patterns depend mainly on the mineralogical composition of the rock matrix.

4.3.2.1. Flow-driven dissolution: [42] Initially, $\Sigma_y Q_z$ (Figure 4c) for sample 1 are uniform with mainly low values of $\sim 1 \times 10^{-2}$ to $\sim 3 \times 10^{-2} \text{ mL min}^{-1}$: Very small regions with medium $\Sigma_y Q_z$ of $\sim 3 \times 10^{-2}$ to $\sim 5 \times 10^{-2} \text{ mL min}^{-1}$ occur locally throughout the fracture. A small region with high $\Sigma_y Q_z$ of $\sim 5 \times 10^{-2}$ to $\sim 7 \times 10^{-2} \text{ mL min}^{-1}$ occurs at low x and z . For sample 2, $\Sigma_y Q_z$ are relatively nonuniform: Low $\Sigma_y Q_z$ (~ 0 to $\sim 1 \times 10^{-2} \text{ mL min}^{-1}$) occur mainly at the center of the fracture (at medium x and z). High $\Sigma_y Q_z$ ($\sim 2 \times 10^{-2}$ to $\sim 3.5 \times 10^{-2} \text{ mL min}^{-1}$) occur mainly at high x . They occur also at low x and low and high z . Medium $\Sigma_y Q_z$ ($\sim 1 \times 10^{-2}$ to $\sim 2 \times 10^{-2} \text{ mL min}^{-1}$) occur in the transition regions between low and high $\Sigma_y Q_z$.

[43] In general, $\Sigma_y Q_z$ remain uniform at high and low Da' . For sample 1 at high Da' the initially high $\Sigma_y Q_z$ at low x and z do not result in preferential dissolution (an excessive increase in fracture volume and thus $\Sigma_y Q_z$). There is no obvious correlation between the excessive increase of $2b$ at high x and the initial $\Sigma_y Q_z$ at that location. For sample 2 at low Da' the initially high $\Sigma_y Q_z$ at high x result in preferential dissolution. There is no obvious correlation between the low and high dissolution rates at low x and medium z

and the initial $\Sigma_y Q_z$ at that location. The initially high $\Sigma_y Q_z$ at low x and medium z correspond to finally low $\Sigma_y Q_z$.

[44] Finally, $\Sigma_y Q_z$ for sample 1 are more uniform with mainly low values of $\sim 1 \times 10^{-2}$ to $\sim 3 \times 10^{-2}$ mL min $^{-1}$. Small regions with medium $\Sigma_y Q_z$ ($\sim 3 \times 10^{-2}$ to $\sim 4 \times 10^{-2}$ mL min $^{-1}$) occur locally throughout the fracture. For sample 2, $\Sigma_y Q_z$ are more uniform. Low $\Sigma_y Q_z$ (~ 0 to $\sim 1 \times 10^{-2}$ mL min $^{-1}$) occur at low x . Medium $\Sigma_y Q_z$ ($\sim 1 \times 10^{-2}$ to $\sim 2 \times 10^{-2}$ mL min $^{-1}$) occur at the inflow region (at low z). High $\Sigma_y Q_z$ ($\sim 2 \times 10^{-2}$ to $\sim 3.5 \times 10^{-2}$ mL min $^{-1}$) occur at high x .

[45] The dissolution patterns (the changes of y_0 , y_1 , and thus $2b$) are generally correlated, to a certain degree, to the flow patterns (the values of $\Sigma_y Q_z$). The flow patterns, in turn, are generally correlated to the fracture morphology (the values of y_0 , y_1 , and thus $2b$). However, several regions with extreme values for the dissolution and flow patterns are not significantly correlated.

4.3.2.2. Buoyancy-driven dissolution: [46] As is evident in Figures 2 and 3 for the horizontal fractures (samples 1 and 2), the dissolution of the lower wall location y_0 is much less rapid than that of the upper wall location y_1 , especially for sample 1 at high number Da' . As mentioned in section 4.3.1, for sample 1 at high Da' , $\langle \nabla_{y_0} \rangle_{xz}$ decreases in magnitude from 0.14 ± 0.09 to 0.0 ± 0.1 and $\langle \nabla_{y_1} \rangle_{xz}$ increases from 0.1 ± 0.1 to 0.2 ± 0.1 , while for sample 2 at low Da' , $\langle \nabla_{y_0} \rangle_{xz}$ and $\langle \nabla_{y_1} \rangle_{xz}$ remain constant in time at $\langle \nabla_{y_0} \rangle_{xz} \approx -0.016 \pm 0.008$ and $\langle \nabla_{y_1} \rangle_{xz} \approx 0.042 \pm 0.006$, respectively. In contrast, for the vertical fracture (sample 3) at low Da' the right and left wall locations y_0 and y_1 , and thus the aperture $2b$, change significantly more rapidly with higher elevation. In fact, the dissolution rates increase approximately linearly with elevation. This indicates that the variation of the dissolution with elevation is the result of free buoyant convection of stratified fluids with density gradients due to solute concentration gradients, i.e., liquids with higher solute concentrations sink, while those with lower concentrations rise. As a consequence, there is considerable vertical asymmetry during fracture development with preferential dissolution at higher elevation (as demonstrated by the experiments with dissolution inhibition for y_0 and dissolution enhancement for y_1) and preferential precipitation at lower elevation. Thus fractures with buoyant dissolution and precipitation selectively develop into overlying rock. Buoyancy gains importance more rapidly as the fractures dissolve more rapidly.

[47] Also, for relatively small concentration gradients, significant buoyancy effects may occur. Therefore fractures may dissolve, become unstable, and collapse far more rapidly than predicted by models that neglect buoyancy. The collapse, even when occurring underneath relatively stable rock, can strongly influence near-surface properties. For example, subsidence features are often closely spaced and arranged in linear patterns related to subsurface fracture intersections [e.g., Cooper, 1986]. Highly soluble, impermeable rock underlain by much less soluble, permeable rock may also be very susceptible to buoyant dissolution. In this case, dissolution of the highly soluble rock is driven by freshwater fed by the permeable rock through vertical conduits that connect both rocks [Anderson and Kirkland, 1980]. Note that the freshwater sources may be relatively distant. This buoyant dissolution may have serious consequences for highly sensitive subsurface sites situated in highly soluble rocks (e.g., mines and radioactive waste repositories).

4.3.2.3. Mineralogy-driven dissolution: [48] The walls dissolve uniformly, except for y_1 of sample 2 at low Da' , where almost no dissolution at low x and medium z is visible. This is

probably due to the mineralogical heterogeneity of the rock matrix (this part of the rock matrix dissolves much less rapidly than the rest).

[49] Chemical analysis of the water-soluble phase of the halite rock samples reveals the mass fractions (mass concentration ratios) of impurities $\rho_{\text{CaSO}_4} / \rho_{\text{NaCl}}$, $\rho_{\text{K}^+} / \rho_{\text{NaCl}}$, $\rho_{\text{Mg}^{2+}} / \rho_{\text{NaCl}}$, and $\rho_{\text{Si}^{2-}} / \rho_{\text{NaCl}}$. The results of the chemical analysis are presented in Figure 6. In addition, the relative halite, anhydrite, calcium carbonate, magnetite, and quartz contents were determined qualitatively by mineralogical analysis.

[50] On the basis of visual observation of color and texture, four distinct types of halite were classified in the source rock from which the samples were cut. Chemical analysis reveals that the samples contain mainly halite with significant traces of calcium sulfates (Figure 6). The white rock is relatively pure halite, the gray rock is less pure, and the brown-gray rock is relatively impure. The dark brown rock is a mixture of halite and calcium sulfates and also contains significant traces of potassium and magnesium, compared to the white and gray samples. The presence of strontium can also be an indicator of the impurity of the halite. Mineralogical analysis reveals that the principal constituent of the white, gray, and brown-gray rocks is halite. The white rock contains trace amounts of anhydrite, while the gray and brown-gray rocks contain larger (although still small) amounts. The principal constituent of the brown rock is anhydrite, with large amounts of halite. None of the rocks contain significant amounts of carbonates or quartz.

[51] Samples from two parts of each of the residual halite samples were analyzed after completion of the experiments. Chemical analysis of the water-soluble phase of these samples reveals the mass fractions averaged for each residual sample (Figure 6). Samples 1 and 3 that were used in the experiments at high Da' are relatively pure halite (equivalent to white and gray halite rock), while sample 2 that was used in the experiment at low Da' is relatively impure halite (equivalent to brown-gray halite rock).

[52] The observed mineralogical heterogeneities of the rock matrix, in combination with the variation of dissolution rates and solubilities for different constituents, can have a strong influence on the dissolution processes. This is especially so if these processes are limited by dissolution reactions. It seems that this effect was observed for y_1 of sample 2 at low Da' with almost no dissolution at low x and medium z . Unfortunately, it was not possible to retrieve sample 2 from the column intact, so a direct, visual inspection could not be performed.

4.3.3. Changing flow patterns. [53] The dissolution patterns in terms of changing flow patterns can be characterized by developing velocity profiles, dynamic flow rates, and stratified flow patterns.

4.3.3.1. Developing velocity profiles: [54] For sample 1 at high Da' the spatial means of the linear correlation coefficients $\langle R^2 \rangle_{xz}$ between the velocity profiles and their best fits increase from 0.3 ± 0.2 to 0.5 ± 0.2 , while for sample 2 at low Da' , $\langle R^2 \rangle_{xz}$ increases from 0.5 ± 0.2 to 0.8 ± 0.2 . Thus, during the dissolution process the velocity profiles become increasingly parabolic, although the transition is less pronounced and less rapid at high Da' . Note that in Figure 4a for sample 2 at low Da' , R^2 increase except in the region near the outflow region at high x and z where R^2 remain constant or decrease. Further, there is no obvious correlation between the nonuniform R^2 and the uniform flow rates $\Sigma_y Q_z$ in Figure 4c.

[55] For sample 1 at high Da' the spatial mean of the y direction offset $\langle \Delta y/b \rangle_{xz}$ decreases in magnitude from -0.4 ± 0.4 to $-0.0 \pm$

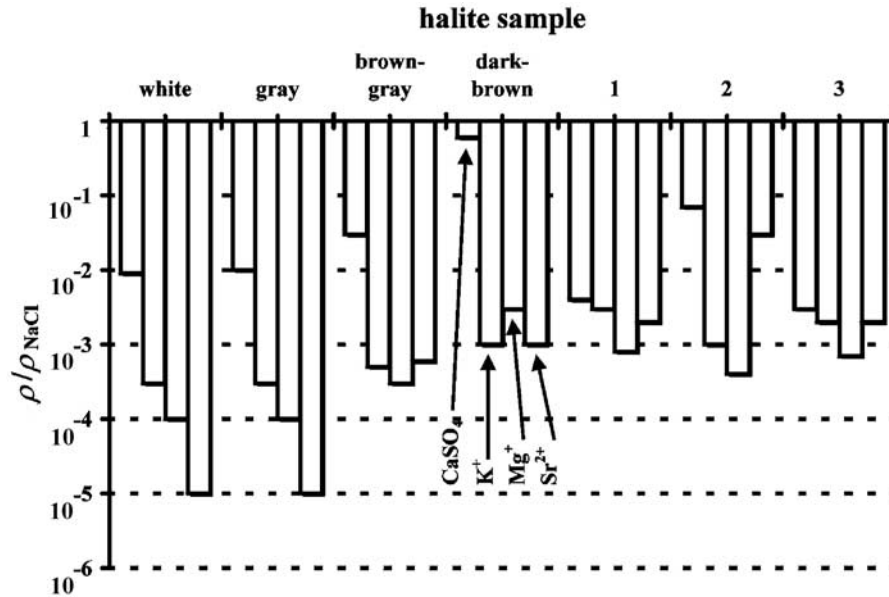


Figure 6. Mass fraction (mass concentration ratio) of impurities ρ/ρ_{NaCl} for different halite samples. The bars represent, from left to right, CaSO_4 , K^+ , Mg^+ , and Sr^{2+} . The four samples at the left are from the host rock, and the three samples at the right are from the dissolution experiments. Owing to the logarithmic scale for ρ/ρ_{NaCl} the results for some of the samples appear to be rather similar. However, the numerical values are distinctly different.

0.1 and that of the absolute y direction offset $\langle |\Delta y/b| \rangle_{xzt} \approx 0.4 \pm 0.3$, while for sample 2 at low Da' , $\langle \Delta y/b \rangle_{xzt} \approx -0.03 \pm 0.02$ and $\langle |\Delta y/b| \rangle_{xzt} \approx 0.08 \pm 0.02$. Thus the velocity profiles change from asymmetric to symmetric with respect to the fracture walls at high Da' and remain symmetric at low Da' .

[56] These results indicate that the velocity profiles become more ideal in terms of the LCL during dissolution when the fracture space (e.g., the apertures and cross-sectional areas) increases, and thus the tortuosity decreases. The fact that velocity profiles may deviate significantly from the LCL and that these deviations change over time (and can diminish due to dissolution) is generally not incorporated in flow models. For example, when the actual velocities near a fracture wall are significantly greater than predicted by flow models, the actual dissolution and precipitation rates may deviate significantly from those predicted by the models. Moreover, these nonideal velocity profiles can significantly influence the transport of solutes.

4.3.3.2. Dynamic flow rates: [57] For sample 1 at high Da and for sample 2 at low Da' the spatial mean of the total flow rate in the xz plane perpendicular to the principal flow (z) direction $\langle \Sigma_{xy} Q_z \rangle_z$ remain virtually constant in space and time: $\langle \Sigma_{xy} Q_z \rangle_z$ increases from 1.2 ± 0.1 to 1.3 ± 0.1 mL min^{-1} and $\langle \Sigma_{xy} Q_z \rangle_z$ remains constant in time at $\langle \Sigma_{xy} Q_z \rangle_{zt} \approx 0.90 \pm 0.03$ mL min^{-1} , respectively. This is because they are fixed by the peristaltic pump: These values for $\langle \Sigma_{xy} Q_z \rangle_z$ are approximately equal to those for $\langle Q \rangle_t$ (see Table 1). However, the local flow rates $\Sigma_y Q_z$ are nonuniform and dynamic, especially for sample 1 at high Da' (Figure 4c).

4.3.3.3. Stratified flow patterns: [58] Buoyancy effects associated with stratified flow are the result of vertical density gradients (in this case due to vertical solute concentration gradients). They are characterized by the dimensionless Rayleigh number, which is a measure of buoyancy versus inertial forces. Stratified flow is stable for low values and unstable for high values. The Rayleigh number is defined here as $Ra = y_s^3 \Delta \rho g / (\mu D_m) = y_s^3 \rho \zeta \Delta c g / (\mu D_m)$, where y_s is the stratified layer thickness, $\Delta \rho$ is the liquid density difference, Δc is the solute concentration difference

over the stratified layer, ζ is the density expansion coefficient for solute concentration, and $g \approx 9.81$ $\text{m}^2 \text{s}^{-1}$ is the gravitational acceleration. To determine Ra , it is assumed that each stratified layer extends over approximately half of the aperture and thus $y_s \approx 0.5 \times 2b = b$. Therefore Ra are directly proportional to the cube of the apertures $(2b)^3$. At $c_{\text{in}}/c_{\text{sat}} = 0$, $\Delta \rho$ is assumed to be equal to that for fully saturated saline solution versus pure water (~ 198 kg m^{-3}) and is also assumed to be equal for pure water versus $\sim 50\%$ saturated saline solution (~ 104 kg m^{-3}) at $c_{\text{in}}/c_{\text{sat}} \approx 0.5$ [Wolf *et al.*, 1975].

[59] Stratified flow patterns are generally highly complex. Some relatively simple cases of stratified flow in single channels have been investigated. Two cases can be distinguished for fully developed, laminar, forced flow in a channel bounded by two planar, horizontal, parallel, smooth plates. The first case is potentially unstable stratified flow with increasing density as a function of elevation. The critical Rayleigh number $Ra_{\text{cr},1}$, which characterizes the transition from stable to unstable flow, was determined by laboratory experiments [e.g., Akiyama *et al.*, 1971]. For channels with infinite lateral extensions it was found to equal $\sim 1.7 \times 10^3$ regardless of the presence of forced flow. For temperature-driven buoyant flow the velocity and temperature profiles for $Ra \approx Ra_{\text{cr}}$ were determined both theoretically [e.g., Nicolas *et al.*, 1997; Mori and Uchida, 1966] and by laboratory experiments [e.g., Akiyama *et al.*, 1971; Mori and Uchida, 1966]. For increasing Ra , longitudinal columnar vortex rolls appear, split, and decrease in size until turbulence occurs. In addition, for channels with vertical lateral boundaries transversal columnar vortex rolls appear below a critical Reynolds number (e.g., ~ 0.3 for water) [e.g., Nicolas *et al.*, 1997]. The second case is stable stratified flow with decreasing density as a function of elevation. On the basis of laboratory experiments [e.g., Akiyama *et al.*, 1971], $Ra_{\text{cr},2}$ was found to be significantly greater than $\sim 10^4$ regardless of the presence of forced flow.

[60] For sample 1 at high Da' the spatial mean of the Rayleigh number $\langle Ra \rangle_{xz}$ increases from $(0.2 \pm 0.2)10^5$ to $(4 \pm 2)10^5$, while for sample 2 at low Da' , $\langle Ra \rangle_{xz}$ increases from $(0.6 \pm 0.3)10^5$ to $(10$

$\pm 3)10^5$. This indicates that the upper stratified layers with density increasing as a function of elevation are probably unstable since $\langle Ra \rangle_{xz} \gg Ra_{cr,1} \approx 1.7 \times 10^3$ for channels with an infinite lateral extension, and longitudinal and transversal columnar vortex rolls may occur. Moreover, the lower stratified layers with decreasing density as a function of elevation are probably also unstable since $\langle Ra \rangle_{xz} \gg Ra_{cr,2} \gg 10^4$. However, the actual stratified flow patterns were not observed with NMRI. This is due to the fact that the timescales of the advection of the vortex rolls are much smaller than the acquisition times of the NMRI images. Instead, the time-averaged flow patterns have been observed. They are expected to be similar to the flow patterns that occur in the absence of stratified flow.

[61] Free buoyant flow with increasing density as a function of elevation, due to salt dissolution at the top of a vertical channel, was observed to be pulsating below some critical channel aperture and to be continuous above [e.g., *Anderson and Kirkland*, 1980]. Stratified flow due to coupled flow and buoyant dissolution and precipitation at the walls of channels (with high densities at the channel walls for dissolution and low densities for precipitation) has not yet been investigated.

[62] Virtually all models of flow in developing fractures completely ignore the presence of stratified flow due to solute concentration (or temperature) gradients. However, this can have a profound affect on the flow patterns and thus on the development of the fracture morphology and cannot be ignored in all cases.

5. Summary and Conclusions

[63] NMRI was successfully applied to measure flow and dissolution patterns in natural, rough-walled, water-saturated halite fractures. To quantify the developing fracture morphology and flow patterns, 3-D NMRI images of water density and flow velocity were used. The results are characterized as a function of the dimensionless Reynolds number for flow, Péclet number for molecular diffusion, Damköhler number for dissolution, and Rayleigh number for buoyancy. Strong interactions between fracture morphology (e.g., fracture surface, volume, and tortuosity), water flow (e.g., preferential flow paths), chemical dissolution (e.g., preferential dissolution regions), and buoyancy (e.g., dissolution rates as a function of wall elevation and orientation) are evident. Chemical and mineralogical analysis reveals that the halite is relatively heterogeneous. The flow patterns are correlated strongly to the fracture morphology, particularly the local apertures and the large-scale wall roughness. The correlations of the dissolution patterns to the fracture morphology, flow patterns, and mineralogical composition of the rock matrix are a function of the overall Damköhler number Da' . At high Da' the dissolution patterns are dominated by the flow patterns, and channeling may occur. In addition, at high Da' , buoyancy effects become important, and the dissolution patterns also depend on the orientation and elevation of the fracture walls. The buoyancy effects result in preferential upward dissolution that may have serious consequences for highly sensitive subsurface sites situated in highly soluble rocks. At low Da' the dissolution patterns depend mainly on the mineralogical composition of the rock matrix.

[64] Summarizing, NMRI has been shown to be a very feasible, powerful, and versatile tool that is able to promote the understanding of the dynamic behavior of coupled flow and dissolution in natural, rough-walled, water-saturated rock fractures. As such, NMRI is the only available tool that is able to directly measure these processes in natural rock fractures. Assumptions underlying existing predictive flow and transport models were examined. Most

models do not take into account nonideal and dynamic velocity profiles, nor the interplay between flow- and mineralogy-driven dissolution processes, and buoyancy effects due to solute concentration gradients. It appears that the coupled flow and dissolution processes are much more complex and unpredictable than commonly assumed, even under simplified conditions. This must be taken into account in conceptual and theoretical predictive models of flow and transport in geological formations with developing fractures. These results can explain subsurface physical processes causing structural instabilities and catastrophic collapse.

[65] **Acknowledgments.** This work was supported by the American Geophysical Union Horton Research Grant and the European Commission (contract ENV4-CT97-0456). The assistance of P. Bendel (Chemical Services Department, Weizmann Institute of Science, Rehovot, Israel) and H. Hemo (Geological Survey of Israel, Jerusalem, Israel) is kindly acknowledged. The authors thank S. Silliman and three anonymous reviewers for their very helpful comments.

References

- Akiyama, M., G. J. Hwang, and K. C. Cheng, Experiments on the onset of longitudinal vortices in laminar forced convection between horizontal plates, *J. Heat Transfer Trans. ASME, Ser. C*, 93(4), 335–341, 1971.
- Alkattan, M., E. H. Oelkers, J. L. Dandurand, and J. Schott, Experimental studies of halite dissolution kinetics, 1, The effect of saturation state and the presence of trace metals, *Chem. Geol.*, 137(3–4), 201–219, 1997.
- Anderson, R. Y., and D. W. Kirkland, Dissolution of salt deposits by brine density flow, *Geology*, 8(2), 66–69, 1980.
- Békri, S., J. F. Thovert, and P. M. Adler, Dissolution and precipitation in fractures, *Eng. Geol.*, 48(3–4), 283–308, 1997.
- Berger, G., M. P. Turpault, and A. Meunier, Dissolution-precipitation processes induced by hot water in a fractured granite, part 2, Modelling of water-rock interaction, *Eur. J. Mineral.*, 4(6), 1477–1488, 1992.
- Berkowitz, B., and J. Zhou, Reactive solute transport in a single fracture, *Water Resour. Res.*, 32(4), 901–913, 1996.
- Bird, R. B., W. E. Stewart, and E. N. Lightfoot, *Transport Phenomena*, 780 pp., John Wiley, New York, 1960.
- Blanpied, M. L., D. A. Lockner, and J. D. Byerlee, An earthquake mechanism based on rapid sealing of faults, *Nature*, 358(6387), 574–576, 1992.
- Brown, S., A. Caprihan, and R. Hardy, Experimental observation of fluid flow channels in a single fracture, *J. Geophys. Res.*, 103(B3), 5125–5132, 1998.
- Cooper, A. H., Subsidence and foundering of strata caused by the dissolution of Permian gypsum in the Ripon and Bedale areas, North Yorkshire, in *The English Zechstein and Related Topics*, edited by G. M. Harwood and D. B. Smith, *Geol. Soc. Spec. Publ. London*, 22, 127–139, 1986.
- Cooper, A. H., Subsidence hazards caused by the dissolution of Permian gypsum in England: Geology, investigation and remediation, in *Geohazards in Engineering Geology*, edited by J. G. Maund and M. Eddleston, *Eng. Geol. Soc. Spec. Publ.*, 15, 265–275, 1998.
- Dijk, P. E., and B. Berkowitz, Precipitation and dissolution of reactive solutes in fractures, *Water Resour. Res.*, 34(3), 457–470, 1998.
- Dijk, P. E., and B. Berkowitz, Three-dimensional flow measurements in rock fractures, *Water Resour. Res.*, 35(12), 3955–3960, 1999.
- Dijk, P. E., and B. Berkowitz, Buoyancy-driven dissolution enhancement in rock fractures, *Geology*, 28(11), 1051–1054, 2000.
- Dijk, P. E., B. Berkowitz, and P. Bendel, Investigation of flow in water-saturated rock fractures using nuclear magnetic resonance imaging (NMRI), *Water Resour. Res.*, 35(2), 347–360, 1999.
- Dreybrodt, W., The role of dissolution kinetics in the development of karst aquifers in limestone: A model simulation of karst evolution, *J. Geol.*, 98(5), 639–655, 1990.
- Dreybrodt, W., Principles of early development of karst conduits under natural and man-made conditions revealed by mathematical analysis of numerical models, *Water Resour. Res.*, 32(9), 2923–2935, 1996.
- Durham, W. B., W. L. Bourcier, and E. A. Burton, Direct observation of reactive flow in a single fracture, *Water Resour. Res.*, 37(1), 1–12, 2001.
- Gong, M., S. Lacote, and A. D. Hill, A new model of acid fracture conductivity based on deformation of surface asperities, paper SPE 39431 presented at Symposium on Formation Damage Control, Soc. of Pet. Eng., Richardson, Tex., 1998.
- Hanna, R. B., and H. Rajaram, Influence of aperture variability on dissolutional growth of fissures in karst formations, *Water Resour. Res.*, 34(11), 2843–2853, 1998.
- Johnson, K. S., Dissolution of salt on the east flank of the Permian Basin in the southwestern U.S.A., *J. Hydrol.*, 54(1–3), 75–93, 1981.

- Johnson, K. S., Evaporite karst in the Permian Blaine Formation and associated strata in western Oklahoma, USA, *Int. Contrib. Hydrogeol.*, 13, 405–420, 1992.
- Kaufmann, G., and J. Braun, Karst aquifer evolution in fractured rocks, *Water Resour. Res.*, 35(11), 3223–3238, 1999.
- Kumar, A. T. A., P. Majors, and W. Rossen, Measurement of aperture and multiphase flow in fractures with NMR imaging, *SPE Form. Eval.*, 12(2), 101–107, 1997.
- Lowell, R. P., P. van Cappellen, and L. N. Germanovich, Silica precipitation in fractures and the evolution of permeability in hydrothermal upflow zones, *Science*, 260(5105), 192–194, 1993.
- Moore, D. E., D. A. Lockner, and J. D. Byerlee, Reduction of permeability in granite at elevated temperatures, *Science*, 265(5178), 1558–1561, 1994.
- Moran, P. R., A flow zeugmatographic interface for NMR imaging in humans, *Magnetic Reson. Imaging*, 1, 197–203, 1982.
- Mori, Y., and Y. Uchida, Forced convective heat transfer between horizontal flat plates, *Int. J. Heat Mass Transfer*, 9, 803–817, 1966.
- Mourzenko, V. V., S. Békri, J. F. Thovert, and P. M. Adler, Deposition in fractures, *Chem. Eng. Commun.*, 148(15), 431–464, 1996.
- Nicolas, X., A. Mojtabi, and J. K. Platten, Two-dimensional numerical analysis of the Poiseuille-Bénard flow in a rectangular channel heated from below, *Phys. Fluids*, 9(2), 337–348, 1997.
- Ohmoto, H., K. Hayashi, K. Onuma, K. Tsukamoto, A. Kitakaze, Y. Nakano, and Y. Yamamoto, Solubility and reaction kinetics of solution-solid reactions determined by in situ observations, *Nature*, 351(6328), 634–636, 1991.
- Raines, M. A., and T. A. Dewers, Mixed transport/reaction control of gypsum dissolution kinetics in aqueous solution and initiation of gypsum karst, *Chem. Geol.*, 140(1–2), 29–48, 1997.
- Turpault, M. P., G. Berger, and A. Meunier, Dissolution-precipitation process induced by hot water in a fractured granite, part 1, Wall-rock alteration and vein deposition process, *Eur. J. Mineral.*, 4(6), 1457–1475, 1992a.
- Turpault, M. P., A. Meunier, N. Guilhaumou, and G. Touchard, Analysis of hot fluid infiltration in fractured granite by fluid inclusions study, *Appl. Geochem. Suppl.*, 1, 269–276, 1992b.
- Vaughan, P. J., D. E. Moore, C. A. Morrow, and J. D. Byerlee, Role of cracks in progressive permeability reduction during flow of heated aqueous fluids through granite, *J. Geophys. Res.*, 91(B7), 7517–7530, 1986.
- Windholz, M. (Ed.), *The Merck Index, an Encyclopedia of Chemicals and Drugs*, 9th ed., 1474 pp., Merck, Rahway, N. J., 1976.
- Wolf, A. V., M. G. Brown, and P. G. Prentiss, Concentrative properties of aqueous solutions: Conversion tables, in *Handbook of Chemistry and Physics*, 56th ed., edited by R. C. Weast, pp. D252–D253, CRC Press, Boca Raton, Fla., 1975.
- Zak, I., The geology of Mount Sedom (in Hebrew with English abstract), Ph.D. thesis, 208 pp., Hebrew Univ. of Jerusalem, Jerusalem, 1967.

B. Berkowitz, Department of Environmental Sciences and Energy Research, Weizmann Institute of Science, Rehovot 76100, Israel. (brian.berkowitz@weizmann.ac.il)

P. E. Dijk, School of Civil and Environmental Engineering, Georgia Institute of Technology, 790 Atlantic Drive, Atlanta, GA 30332-0355, USA. (peter.dijk@ce.gatech.edu)

Y. Yechieli, Geological Survey of Israel, 30 Malkhei Israel Street, Jerusalem 95501, Israel. (yechi@mail.gsi.gov.il)